

RESEARCH ARTICLE

Gravity enables self-assembly

Ivan Grega¹  | Angkur J. D. Shaikeea¹ | Haydn N. G. Wadley² |
Vikram S. Deshpande¹ 

¹Department of Engineering, University of Cambridge, Cambridge, UK

²Department of Material Science & Engineering, School of Engineering and Applied Science, University of Virginia, Charlottesville, Virginia, USA

Correspondence

Vikram S. Deshpande, Department of Engineering, University of Cambridge, Trumpington Street, Cambridge CB2 1PZ, UK.
Email: vsd@eng.cam.ac.uk

Funding information

Army Research Office, Grant/Award Number: W911NF-19-1-0075

Abstract

Crystallization of granular assemblies has broad implications for rapid and scalable creation of architected materials with applications ranging from structural materials to microarchitected battery electrodes. While significant advances have been made in understanding colloidal self-assembly at nano to micro scale, the governing mechanisms for organization of dry assemblies of hard spheres remain unclear. Here, we investigate crystallization of mono-size hard spheres with and without imposed vibration. Using X-ray computed tomographic analysis coupled with discrete-element simulations, we unravel the roles of gravity and imposed vibration on the three-dimensional self-assembly of the dry spheres. We use these insights to introduce gravity-mediated epitaxial crystal growth with slow pouring of balls on seeding templates. Contrary to vibration-induced crystallization, this method can form large single crystals with both close-packed and rather surprisingly, nonclose-packed metastable particle arrangements. Our results provide insight for the scalable manufacture of defect-free granular assemblies that can be used as space-holding templates to manufacture cellular materials, such as inverse opals and other related topologies.

Key points:

- Self-assembly of hard spheres is a critical step for the scalable manufacture of microarchitected solids.
- Via a combination of vibration experiments, 3D X-ray tomographic observations, and simulations, we elucidate the critical role of gravity in the self-assembly of hard spheres.
- We design seeding templates that can not only induce the self-assembly into stable close-packed crystal structures but also rather counterintuitively into metastable single crystal structures.

KEYWORDS

discrete element method, granular mechanics, inverse opals, self-assembly

This is an open access article under the terms of the [Creative Commons Attribution](https://creativecommons.org/licenses/by/4.0/) License, which permits use, distribution and reproduction in any medium, provided the original work is properly cited.

© 2022 The Authors. *Natural Sciences* published by Wiley-VCH GmbH.

INTRODUCTION

Low-density cellular architected materials with a range of topologies, parent materials, and length scales have been shown to attain unique combinations of properties and fill the so-called white spaces in the Ashby material property maps.¹ Most of these materials with complex microarchitectures are manufactured by additive² or other relatively slow and expensive processes,³ limiting their deployment in large-scale structural applications. A notable exception is the inverse opal architecture manufactured by a variety of colloidal assembly routes⁴⁻⁶ for applications ranging from photonic crystals^{7,8} to bat-

tery electrodes.^{9,10} Figure 1a illustrates the key steps in the manufacturing process of inverse opal crystal: (1) spherical particles are self-assembled into a close-packed crystal and sintered together, (2) second material is deposited into the voids, and (3) the particles are etched out.⁹⁻¹¹ Nickel-based inverse opals manufactured in this way have shown exceptional mechanical properties with hardness exceeding 2 GPa.¹¹ However, while the hardness of these materials is exceptional, they suffer from a low tensile strength due to numerous defects that originate from the original self-assembly arrangement of mono-size spheres (Figure 1b). This study focuses on understanding the dry assembly of mono-size hard spheres: the arrangement of such

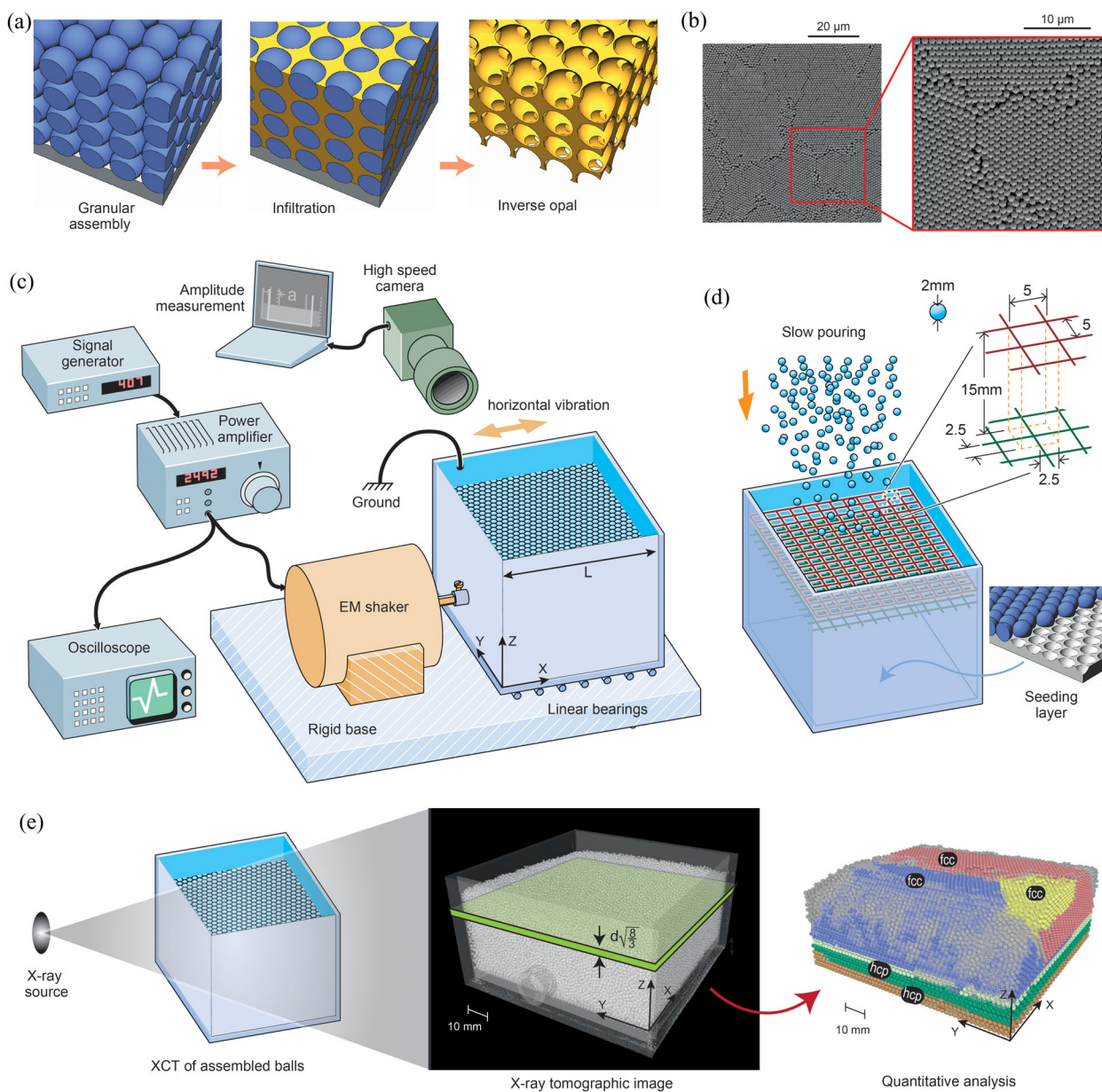


FIGURE 1 (a) Sketch of the process of constructing inverse opals from a self-assembled arrangement of mono-size spheres. (b) Micrographs showing defects in self-assembled spin-coated thin films of PMMA spheres. (c) Schematic of the setup used for vibration-induced assembly of mono-size spheres (balls). (d) Schematic of the setup for epitaxial crystal growth from a seeding layer. Pouring of balls into the box is randomized by a double-layer wire mesh arrangement. (e) XCT was used to analyze the granular assembly, including the 3D crystal structure and defects. A slab of thickness $d\sqrt{8/3}$ is also marked and used to define the local crystallinity fraction $\phi(z)$ at a height z in the box

granular assemblies is a problem of fundamental scientific interest and encountered in nature as well as numerous contemporary sectors, such as the manufacture of inverse opal architected materials. Colloidal suspensions comprising mono-size spheres crystallize via sedimentation with¹² and without a seeding template^{13–15} and under oscillatory motions.¹⁶ Light-scattering¹⁶ and X-ray measurements¹⁵ have been used to establish packing arrangements and inevitably the arrangements comprise random stacks of close-packed horizontal planes. Consequently, a mixture of face-centered cubic (fcc) and hexagonal close-packed (hcp) structures ensues, and single crystals are not obtained. Manufacture of inverse opals via electrodeposition is sometimes simplified using dry templates, and our focus here is on the crystallization of dry assemblies of mono-size hard spheres. The hard-sphere assumption is appropriate for sizes typically $> 10 \mu\text{m}$ when interparticle attractive/repulsive forces due to electrostatic and other such interactions are negligible.

There exists a vast literature on the random packing of mono-size spheres starting from the early work of Scott^{17,18}; see Ref. [19] for a detailed review. Owe Berg and McDonald²⁰ were the first to report that such random assemblies crystallize under imposed vibration. While Berg et al.²⁰ analyzed packings by pouring water into the assembly and then freezing it to enable the sectioning and imaging of the assembly, nearly all subsequent experimental studies^{21–23} use packing fraction measurements to gauge the level of crystallization. Mono-size spheres pack to maximum 74% volume fraction in a fully crystalline fcc or hcp arrangement, while the dense random packing density is around 64%. Thus, an increase in packing fraction serves as a surrogate measure for the level of crystallization but is inaccurate as it lacks information on microstructural defects. Such defects have only a minor effect on the overall volume fraction but play a crucial role in the properties of inverse opals made using these granular assemblies as templates.¹¹ Nonetheless, such experimental studies have provided data that suggest that sphere size, vibration frequency, and amplitude all govern the level of crystallization. However, such observations have provided only very limited insight into the physical mechanisms that induce crystallization.

The discrete element method (DEM) has also been employed to investigate crystallization of dry granular assemblies.^{25–28} These simulations have been used to propose a range of crystallization mechanisms, including crystal growth, whereby two adjacent crystals coalesce and epitaxial growth from existing nuclei.²⁵ The notion of a seed is present in numerous studies with {111} and {100} seeding planes used to grow fcc crystals,²⁶ while friction between the walls and the spheres has also been shown to initiate crystallization.²⁸ Relatively small systems comprising between 2500 and 10k spheres were considered in these investigations with the role of boundaries of the container, therefore, playing an important role. DEM simulations have also been used to try and understand the role of the vibration parameters. Combinations of experiments and DEM simulations suggest that two nondimensional groups govern the level of crystallization: (1) the vibration intensity^{29,30} $a\omega^2/g$, where a is the vibration amplitude and ω is the angular frequency, while g is the acceleration due to gravity, and (2) the normalized velocity³¹ defined as $a\omega/\sqrt{gd}$, where d is the diameter of

the spheres. There is no agreement in the literature on whether one or both parameters govern crystallization, and we attribute this to the fact that these studies used packing fraction to estimate the level of crystallization.

Experimental investigations have also shown that container geometry and seeding enhances crystallization of dry assemblies of spheres. Schemes employed include using triangular containers to build crystals layer-by-layer³² and using seeding plates to grow fcc crystals in different orientations.³³ These investigations were restricted to visualizing the arrangements from the sides of the container, and thus, unable to infer arrangements within the bulk. Moreover, the mechanisms that help seeds induce crystallization in these granular systems remain unclear: unlike atomic crystals, there are no long-range interparticle forces, and in fact, all interparticle forces are negligible under static conditions.

This study focuses on understanding the crystallization of dry granular assemblies of mono-size hard spheres as not only a problem of fundamental scientific and practical interest but also as a simple system that will provide broader insights into crystallization mechanisms. Two cases were considered: (1) vibration-induced crystallization of an initially amorphous assembly (Figure 1c) and (2) growth from a base seeding layer with and without vibration (Figure 1d). A combination of experiments, including visualization via X-ray computed tomography (XCT) (Figure 1e) and discrete element simulations (Materials and Methods), was used to develop a mechanistic understanding of the mechanisms of crystallization. In the absence of seeding, vibration induces crystallization resulting in horizontal close-packed {111} planes. Approximately equal fractions of hcp and fcc grains develop separated by coherent boundaries as well as amorphous regions. Combining experiments and simulations, we discover that the ratio of an imposed horizontal acceleration to the vertical gravitational acceleration uniquely governs the level of crystallization. We show that gravity can be exploited to induce growth of large crystals. We find that a {100} seeding layer has a gravitational energy landscape with a unique family of equilibrium sites, allowing the growth of both fcc and a kinetically trapped nonclose-packed bcc single crystal arrangements. By contrast, the close-packed {111} seeding layer has two families of equilibrium sites in the gravitational potential energy landscape, and this results in a mixture of hcp and fcc grains. No seeding arrangement allowed for the growth of an hcp single crystal although we demonstrate that seeding via a horizontal prismatic {10 $\bar{1}$ 0} plane restricts the granular arrangement to comprise only hcp grains.

RESULTS AND DISCUSSION

Three-dimensional visualization and analysis of vibration-induced crystallization

We employed 100k spherical cellulose acetate balls* with a nominal diameter $d = 2 \text{ mm}$ that were coated to minimize electrostatic

* Precision Plastic Ball Co Ltd, U.K.

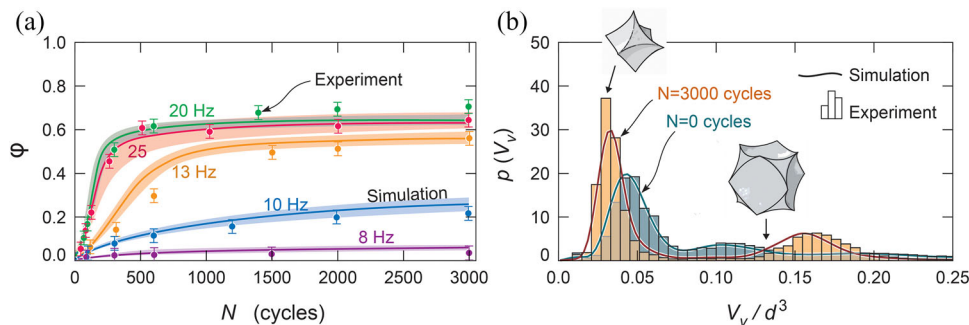


FIGURE 2 (a) Measurements and predictions of the evolution of the total crystallinity fraction ϕ in the box with number of cycles N for five selected vibration frequencies f . The error bars on the measurements indicate the scatter over three different experiments, while the shaded regions show the variability of the predictions over the simulations with six different initial random arrangements. (b) Measurements and predictions of the probability density of the normalized void volumes V_v/d^3 in the box subjected to shaking at $f = 20$ Hz. The distributions are shown prior to shaking ($N = 0$) and at steady state at $N = 3000$. The volumes of the tetrahedral and octahedral holes in the hcp/fcc structures are marked to aid the interpretation of the two peaks in the $N = 3000$ distribution. In both (a) and (b), the vibration amplitude $a = 2$ mm

interactions (Materials and Methods and Figure S1). These balls were randomly assembled into an open-top Perspex box with a square base of length $L = 12$ cm. The box was aligned with the Cartesian coordinate system with the gravity acting in the negative Z -direction and vibrated in the $X - Y$ plane along the X -direction. It was found that the horizontal harmonic oscillatory motion induced crystallization in the system (see XCT data in Video S1). We first report detailed observations for the reference case of oscillation at $f = 20$ Hz and an amplitude of $a = 2$ mm (i.e., $a/d = 1$) and then discuss the effect of the loading parameters, including frequency. Measurements of the evolution of the total crystallinity fraction ϕ (extracted from the XCT and defined as the ratio of all the balls that form any type of crystalline structure to the total number of balls; see Materials and Methods) with number of cycles N are included in Figure 2a (error bars show variability over three different experiments). The data show that the balls in the box crystallize into a steady-state structure for $N > 1000$. Another, and maybe more discerning indicator of the crystallization of the structure is the distribution of void sizes within the crystal. Recall that for a pure fcc or hcp crystal with no defects, there exist only octahedral or tetrahedral voids. Thus, for these perfect close-packed crystals, we would anticipate a discrete void size distribution comprising tetrahedral and octahedral voids of volumes $V_T \approx 0.026d^3$ and $V_O \approx 0.132d^3$, respectively, with the tetrahedral voids twice as numerous as the octahedral voids. Measurements of the probability density of the normalized void volume distributions V_v/d^3 prior to shaking ($N = 0$) are included in Figure 2b for $f = 20$ Hz, where V_v is the void size measured using the foam/powder (FP) analysis (Materials and Methods). The distribution has one distinct peak corresponding to void size a bit larger than the tetrahedral void. The lack of two distinct peaks, which would correspond to tetrahedral and octahedral voids, confirms the high degree of randomness in the granular packing. The corresponding void volume distribution after shaking to $N = 3000$ (i.e., the steady state for $f = 20$ Hz seen in Figure 2a) is also included in Figure 2b. Now intriguingly, we observe a bimodal distribution: the first peak correlates well with the volume of the tetrahedral voids, while the second peak is lower and occurs at a volume larger than the octahedral void

volume. This strongly suggests that although the ball arrangements have a high degree of vibration-induced crystallinity, the crystal structure is defected.

Visualization of crystal defects

To illustrate the formation of crystalline structures and associated defects, we visualize the 3D arrangements using XCT (Figure 3a) and include in Figure 3b visualizations of horizontal sections through the box at selected numbers of cycles N (vertical sections shown in Figure S2a). With z denoting the co-ordinate along the Z -direction, we define $\bar{z} \equiv z/H$, where $H = M\pi d^3/(6\bar{\rho}L^2)$ is the height of the assembly of a perfect fcc packing of $M = 10^5$ balls with $\bar{\rho} = 0.74$ being the fcc packing fraction, while $\bar{x} \equiv x/L$ and $\bar{y} \equiv y/L$ are the fractional co-ordinates in the X and Y -directions, respectively. Balls in the XCT images in Figure 3b are colored by their local crystal structure. Prior to the shaking of the box, the arrangement of the balls is nearly completely amorphous. Vibratory motion in the X -direction resulted in the development of crystallinity (sequence in Figure 3b). Steady state is observed in the slices at $N = 3000$, whereby the fcc and hcp crystal structures dominate (see Video S2). The approximately equal split in the fcc and hcp crystal structures will be explained more clearly in Section “Improving crystallization via seeding layers” but at this point, it suffices to say that gravity creates a strong tendency for the horizontal plane to be close-packed (see Video S1). However, these close-packed horizontal planes can either be arranged in an “ABAB” arrangement (i.e., every other close-packed layer balls have the same (X, Y) co-ordinates) or “ABCABC” arrangement (i.e., every third close-packed layer balls have the same (X, Y) co-ordinates), and this creates an approximately equal mix of hcp and fcc structures.

While the images in Figures 3b and S2a indicate the types of crystal structures that form, the mixture of fcc and hcp crystals creates grain boundaries and associated defects. To understand these defects, we show in Figure 4 the XCT reconstructed grain structure at

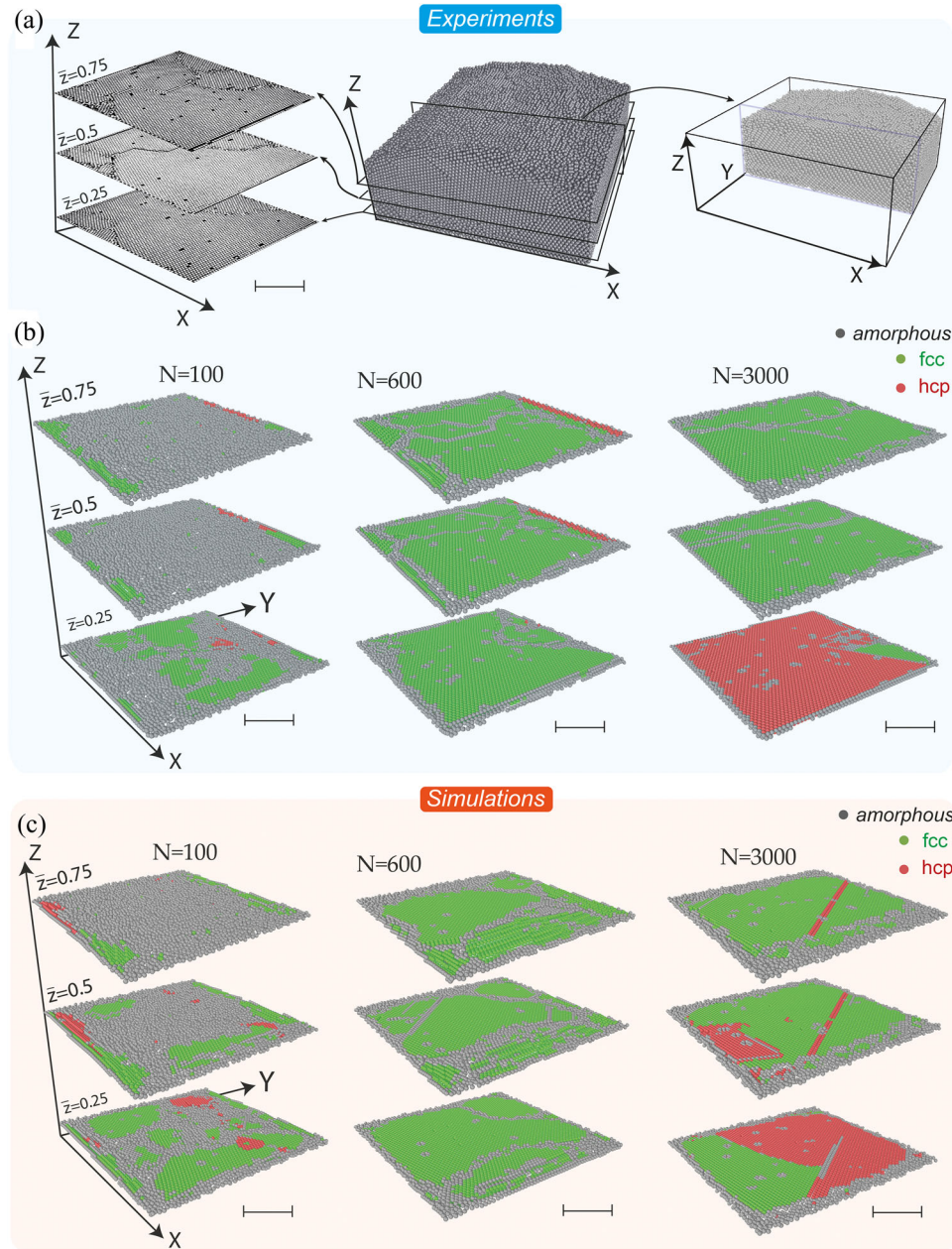


FIGURE 3 (a) Visualization of the arrangement of the balls via X-ray computed tomography (XCT). (b,c). Sections in the $X - Y$ plane at normalized positions $\bar{z} = 0.25, 0.5$, and 0.75 after shaking to $N = 100, 600$, and 3000 cycles at a frequency $f = 20$ Hz with an amplitude $a = 2$ mm. The balls are colored by the crystal structure they are deemed to lie within. The hcp and fcc structures dominate along with amorphous regions. XCT observations with the XCT images of the balls colored via post-processing are shown in (b), while in (c), we include corresponding predictions. The XCT images in (a) correspond to $N = 600$ in (b). Scale bar 30 mm

$N = 3000$. To improve the visualization, we have excluded 10 layers of balls from the four sides and five layers from the top of the box to focus attention on the central crystallized region within the box. As known from Figures 3b and S2a, two crystal types dominate but more importantly, the different hcp and fcc grains are all in the same orientations (Figure 4b) with the close-packed plane being horizontal. What then demarcates the different grains, including two grains with the same crystal structure? Four different types of boundaries are observed in the assembly at steady state: three types of coherent grain bound-

aries and an amorphous zone between adjacent grains (Figure 4a). The coherent boundaries are (Figure 4a):

- (i) An hcp/hcp boundary: Here, two identical hcp grains are slipped half a ball spacing apart, that is, the ABAB arrangement is broken by the existence of a close-packed C layer, which then again alternates as ACAC to form another hcp crystal.
- (ii) An hcp/fcc boundary: This boundary is again a boundary, where the two adjacent close-packed layers have slipped half a ball

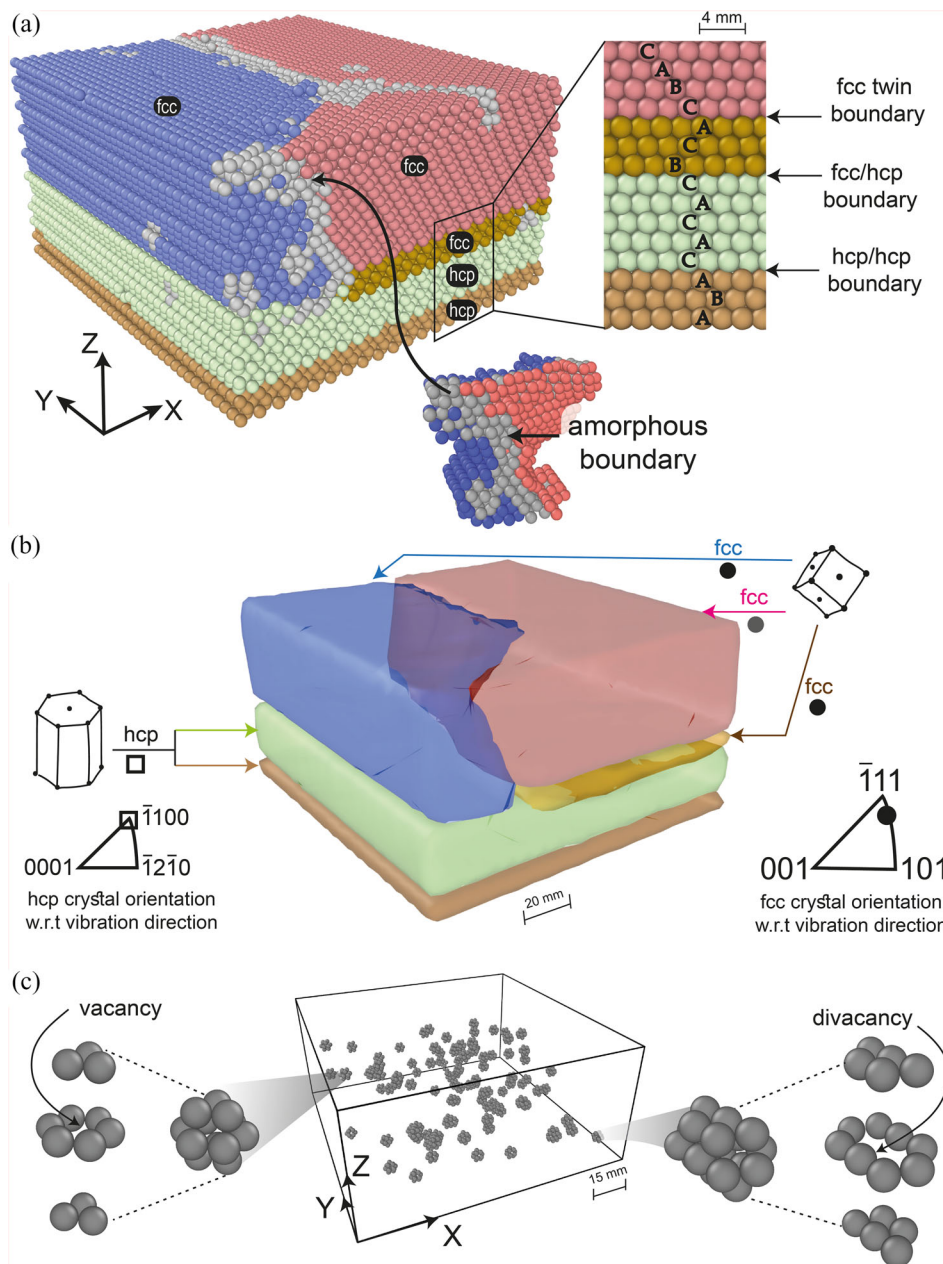


FIGURE 4 XCT reconstructed image of the arrangement of balls after shaking to $N = 3000$ cycles at a frequency $f = 20$ Hz with an amplitude $a = 2$ mm. (a) Reconstruction with the individual balls shown and coloured in a post-processing step to illustrate different types of grain boundaries. (b) The XCT reconstruction with the grains shaded translucently to help visualization of the grain boundaries within the volume. The fcc and hcp unit cells along with their orientations are also sketched. The crystal orientation with respect to vibration direction is shown in the inverse pole figures. (c) Distribution of mono and divacancy structures observed in experiments. The zoom-ins show the structures of these vacancies as observed through the XCT data

spacing such that the ACAC arrangement is interrupted by the existence of a close-packed B layer. However, now the arrangement continues in an ABC arrangement to form an fcc crystal.

- (iii) An fcc/fcc twin boundary: This is a classical coherent twin boundary between two otherwise identical grains.

The fourth type of boundary is an amorphous region separating two identically oriented fcc grains as seen in Figure 4a. This amorphous region presumably developed because two closely situated fcc crys-

tals grew from the bottom but were slightly displaced with respect to each other (as later discussed in Section “Improving crystallization via seeding layers”). The region between these two crystals can then only be filled by an amorphous arrangement of the balls as coalescence of two large fcc grains would require their complete reconstruction. In Section “Growth of the crystal structure”, we will discuss the kinetic barriers to crystallization, where it will become apparent that just large-scale recrystallization is highly unlikely in this granular system.

In addition to defects, such as the grain boundaries discussed above, another ubiquitous crystalline defects, viz., vacancies, are also observed. XCT visualization of vacancies after 3000 cycles included in Figure 4c reveals the existence of both mono and divacancies. These vacancies have volumes much greater than the tetrahedral and octahedral holes (a mono vacancy has a volume $\approx 1.524 d^3$), and thus, their count falls outside the scale of the void size distributions shown in Figure 2b. However, it is such vacancies combined with the voids in the amorphous regions, voids along grain boundaries and voids near the side walls of the box that contribute to the continuous distribution of void volumes seen in Figure 2b.

Growth of the crystal structure

While the evolution of the crystal structure with cycles can be visualized through the slices shown in Figures 3b and S2a, these slices are insufficient to understand the mechanism of crystal growth. Typically, atomic crystals are grown from a seed with crystallization propagating through the material as a front³⁴: does a similar process occur in such granular assemblies, where long-range interparticle forces are absent? To understand the mechanism of crystal growth, we define a local crystallinity fraction $\hat{\phi}(z)$ as the crystallinity in a slab centered at $Z = z$ with thickness $d\sqrt{8/3}$ (which corresponds to the thickness of two close-packed layers; see Figure 1e). Measurements of $\hat{\phi}(\bar{z})$ as a function of the normalized position \bar{z} are shown in Figure 5a for the reference case of shaking at $f = 20$ Hz ($a = 2$ mm), and for selected values of N (error bars show variability over six different experiments). The assembly begins to crystallize at the base ($\bar{z} = 0$) with the level of crystallinity first increasing at the base followed by crystallization near the top of the box as N increases. However, no sharp crystallization front that moved upward through the box was observed.

Now, consider the case of vibration at a lower frequency of $f = 13$ Hz (Figure 5b) with the reference amplitude ($a = 2$ mm). Crystallization now mainly initiates near the top surface at $\bar{z} \approx 1$ and then spreads toward the bottom, although some crystallization very near the bottom surface is also seen early in the vibration history. Another key difference is the rate of crystallization: comparing Figures 5a,b, we see that while the final steady-state crystallinity was attained at $N \approx 600$ for shaking at $f = 20$ Hz, nearly 3000 cycles were needed to attain a slightly lower steady-state crystallinity at $f = 13$ Hz. This observation is better summarized in Figure 2a, where we include measurements of the total crystallinity fraction ϕ in the box as a function of N for selected values of f . The data in Figure 2a suggest the existence of a critical frequency $f = f_{\text{crit}} \approx 20$ Hz such that both the rate of crystallization and the final steady-state value of ϕ_{ss} are approximately independent of f for $f > f_{\text{crit}}$. However, both ϕ_{ss} and the rate of crystallization decrease with decreasing f for $f < f_{\text{crit}}$.

We note that the switch in the crystallization mode from being only growth upward from the base to being mainly growth downward from the top surface also occurs at $f \approx f_{\text{crit}}$. This provides some hints for an understanding of the mechanism of crystallization. The XCT image of the layer of balls on the bottom surface ($\bar{z} = 0$) of the box prior to shaking ($N = 0$) is shown in Figure 5c. Patches with randomly oriented

close-packed arrangements are evident, although there is a high density of vacancies, grain boundaries, and amorphous regions between the crystalline patches. The corresponding reconstructions at $N = 100$ for $f = 20$ Hz (Figure 5d) and 13 Hz (Figure 5e) illustrate that grain growth has occurred in both cases with the density of grain boundaries, the vacancy concentration, and the amorphous fraction all reducing, although this is more evident for $f = 20$ Hz. This crystallized bottom layer then acts as a seed with crystal growth occurring from this seed via a gravity-controlled mechanism. This mechanism differs from crystallization in atomic systems in at least the two following ways:

- (i) The shaking of the box provides energy and induces the random vibrations required to cause the rearrangement of the balls into a maximum entropy arrangement.³⁵ In atomic systems, the equivalent vibrations are a result of the finite temperature of the system.
- (ii) Gravitational energy is the only contributor to the potential energy of the static granular system as the balls do not have any electrostatic or other interactions. Thus, there exists a gradient in potential energy of the system along the Z -direction. In atomic systems, atomic bond forces dominate the potential energy with gravity playing a negligible role.

This role of gravity is critical in understanding the low- and high-frequency crystallization process. To crystallize following the seed induced by the bottom layer, the rearrangement of the balls near $\bar{z} = 0$ requires the balls to ride up on each other (Figure 5f). Thus, work needs to be done against gravity to lift balls (colored pink in Figure 5f) lying in the higher layers. Recall that vibration of the box results in the balls acquiring an acceleration $\propto a\omega^2$, where $\omega \equiv 2\pi f$ is the angular frequency due to the imposed vibration. For shaking at $f > f_{\text{crit}}$, this acceleration is sufficient to overcome the gravitational barrier and crystallization follows the seed of the bottom layer in a highly efficient manner with a consequent high crystallization rate. On the other hand, for $f < f_{\text{crit}}$, the acceleration is insufficient for balls near the bottom that are constrained by the pressure exerted by the higher up layers. However, recall that the maximum entropy state³⁵ is the close-packed arrangement, and thus, there is a strong tendency for the balls to rearrange and crystallize into either the fcc or hcp crystal structures. Therefore, layers at the top of the assembly begin to crystallize as they are relatively unconstrained; see sketch in Figure 5f. However, this process is inefficient as these top layers do not have a stable seed to follow, and the process of crystal growth is significantly slower. Simulations presented in Section “Simulations uncover the role of gravity and the mechanisms of crystallization” will further clarify the role of the frequency f , and a more in-depth investigation into the role of the bottom seeding layer in Section “Improving crystallization via seeding layers” will further clarify the crystallization process.

Simulations uncover the role of gravity and the mechanisms of crystallization

To uncover the mechanism of the crystallization process, we use the discrete element soft-contact approach first introduced by Cundall and

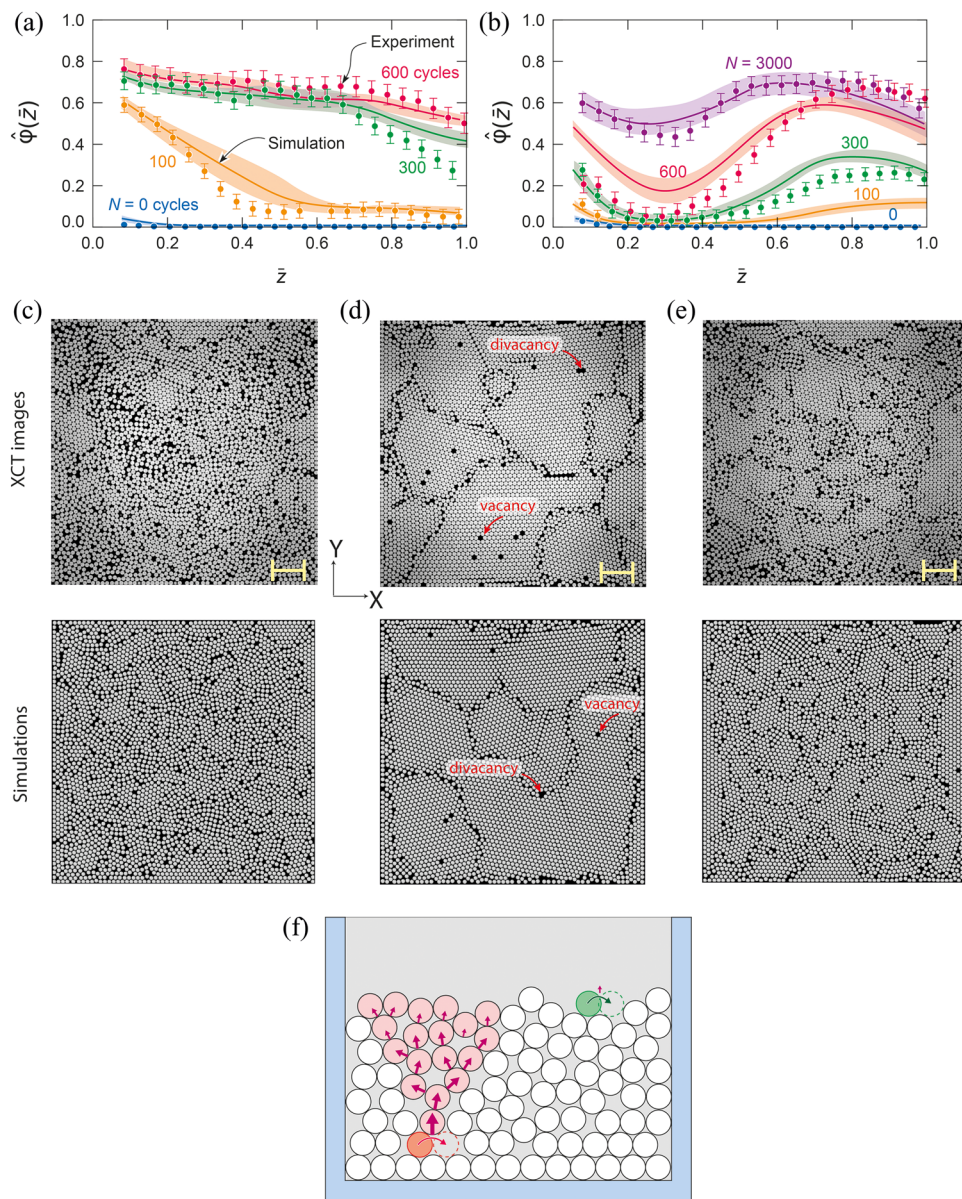


FIGURE 5 (a,b) Measurements and predictions of the local crystallinity $\hat{\phi}$ within a slab of thickness $d\sqrt{8/3}$ (Figure 1e) as a function of the normalized Z co-ordinate $\bar{z} \equiv z/H$. Results are shown for selected number of cycles N for vibration of the box at an amplitude $a = 2$ mm at a frequency (a) $f = 20$ Hz and (b) $f = 13$ Hz. The error bars on the measurements indicate the scatter over six different experiments, while the shaded regions show the variability of the predictions over the simulations with six different initial random arrangements. (c–e) XCT images and corresponding simulations that show the bottom layer ($\bar{z} = 0$) of balls in the box (c) prior to vibration ($N = 0$) and after $N = 100$ cycles for vibration at a frequency (d) $f = 20$ Hz and (e) $f = 13$ Hz and amplitude $a = 2$ mm. Scale bar 15 mm. (f) Sketch illustrating the need to lift a series of balls to rearrange balls near the base of the box, while balls at the top of the box can be rearranged without disturbing other balls. The arrows indicate the lifting forces

Strack³⁶ and implemented in the simulation tool LAMMPS³⁷ (package GRANULAR). The simulations were conducted in two steps: (1) simulation of the pouring under gravity of M balls into a rigid open-top box to create an initial dense random packing of balls and (2) shaking of the box to induce crystallinity; see Materials and Methods. Video S3 shows the process of pouring and the initial phase of shaking.

Numerical predictions of the evolution of crystallinity fraction ϕ with N are shown in Figure 2a (shaded bands indicate the variabil-

ity in predictions for six different initial random arrangements of the balls) and show excellent agreement with the measurements not only for the evolution of crystallinity with cycles but also the fact that steady-state crystallinity decreases below a critical frequency. Correspondingly, there is good agreement between the measurements and predictions of the distribution of void sizes in the assembly of balls (Figure 2b). While the results of Figure 2 show that there is good agreement between measurements and predictions for the effect of shaking on statistical measures of the arrangement of the balls, it is

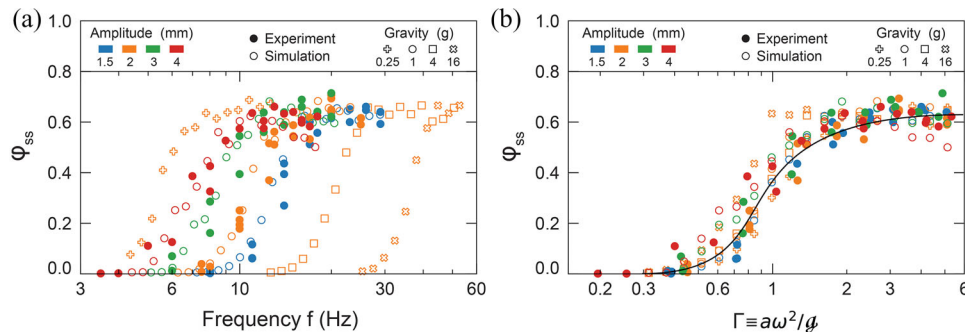


FIGURE 6 (a) Measurements and predictions of the variation of the steady-state crystallinity fraction φ_{ss} in the box as a function of vibration frequency f . Measurements are for a range of amplitudes a , while the predictions include these amplitudes as well as varying levels of the acceleration due to gravity g for an amplitude $a = 2$ mm. (b) A replot of all the data from (a) as a function of the vibration intensity $\Gamma \equiv a\omega^2/g$ to illustrate that the data collapse onto a single master curve that is sketched in.

instructive to understand the nature of these predictions in terms of local arrangements. Analogous to the XCT observations, we include in Figure 3c and Figure S2b horizontal and vertical sections, respectively, through the box showing predictions of the local arrangements. The predictions and observations of the distribution of fcc and hcp crystal structures do not exactly match. This is unsurprising since these local arrangements are statistical in nature. The repeat experiments and simulations have different arrangements of the crystal structures to those seen in Figure 3 and Figure S2 but nearly identical values for statistical measures, such as φ ; recall the variability seen in Figures 2a and 5a,b. Furthermore, consistent with the XCT observations, the predictions show a near equal mix of fcc and hcp grains and the existence of mono and divacancies within the crystals.

The simulations with different shaking frequency are key in understanding the mechanisms of crystallization. We first consider the differences in the evolution of crystal growth for $f = 20$ and 13 Hz, seen in Figure 5a,b, respectively. The predictions accurately capture the measurements, including the important fact that crystallization initiates at the base of the box ($z = 0$) for the $f = 20$ Hz case with the crystal growing upward, while the reverse occurs in the $f = 13$ Hz case. The reasons for this were discussed qualitatively in Section “Growth of the crystal structure” and relate to the acceleration $a\omega^2$ of the box. (Video S4 contrasts the growth of crystalline regions for the two frequencies.) We now proceed via a combination of experiments and simulations to investigate the role of the inputted power that induces vibrational motion of the balls, which, in turn, permits their rearrangement into a crystal structure.

Measurements of the overall steady-state crystallinity fraction φ_{ss} in the box are included in Figure 6a as a function of the frequency f for selected values of amplitudes in the range $1.5 \text{ mm} \leq a \leq 4 \text{ mm}$. The behavior is overall similar for all amplitudes with very low levels of crystallinity developing below a critical frequency f_{crit} with φ_{ss} rising rapidly above f_{crit} before plateauing out at $\varphi_{max} \approx 0.7$. While φ_{max} is reasonably independent of a , the critical frequency f_{crit} decreases with increasing a . This seems consistent with the idea that a critical acceleration is required to initiate crystallization. To understand this critical level, we restrict attention to the case of a given box with a fixed number of balls all of diameter d and a given set of material proper-

ties. Thus, the only variables of interest are the loading parameters, viz, amplitude a , angular frequency $\omega \equiv 2\pi f$, and acceleration due to gravity g . Within the hard sphere approximation, dimensional analysis then specifies that the steady-state crystallinity fraction φ_{ss} is uniquely specified by the nondimensional parameter $\Gamma \equiv a\omega^2/g$ (referred to as vibration intensity), the ratio a/d , and the friction coefficient μ between the balls. The measurements were conducted under normal gravitational conditions of $g = g = 10 \text{ ms}^{-2}$, and we replot the measured data of Figure 6a as φ_{ss} versus Γ in Figure 6b. To within the expected statistical variability, the measurements collapse onto a single master curve demonstrating that crystallization for a given system is purely a function of the imposed acceleration and independent of a/d (μ was not varied in the measurements).

Of the three parameters comprising vibration intensity $\Gamma \equiv a\omega^2/g$, we have managed to experimentally verify the effect of amplitude and frequency. Since changing g in the experiments is challenging, we resort to numerical simulations to probe its effect. First, consider the predictions of the φ_{ss} as a function of f for the experimentally investigated range of amplitudes $1.5 \text{ mm} \leq a \leq 4 \text{ mm}$ with $g = g = 10 \text{ ms}^{-2}$ (Figure 6a). The predictions are generally in agreement with the measurements and do not collapse onto a single curve. We also include in Figure 6a predictions with $a = 2$ mm and the acceleration due to gravity in the range $0.25g \leq g \leq 16g$ (i.e., $0.25 \leq \alpha \equiv g/g \leq 16$). The predictions now widely scatter with f_{crit} increasing with increasing g . All the predictions are replotted in Figure 6b but now with φ_{ss} as a function of Γ . The predictions (to within scatter associated with statistical uncertainty in φ_{ss}) collapse onto a single master curve confirming that the ratio of the imposed acceleration to the gravitational acceleration governs the level of crystallinity at steady state with a/d having a minor influence. The physical interpretation of this finding is that rearrangement of the balls into the high-entropy fcc or hcp packing requires the balls to ride-up on each other as shown in Figure 5f. To do this, the balls require an acceleration to overcome gravity, and this acceleration is provided by the acceleration $a\omega^2$ imposed to the box. Thus, the critical vibration intensity at which crystallization commences is $\Gamma \approx 1$; see Figure 6b. (The only material parameter that influences the master curve in Figure 6b is the friction coefficient μ between the balls; see Figure S3 and Materials and Methods.)

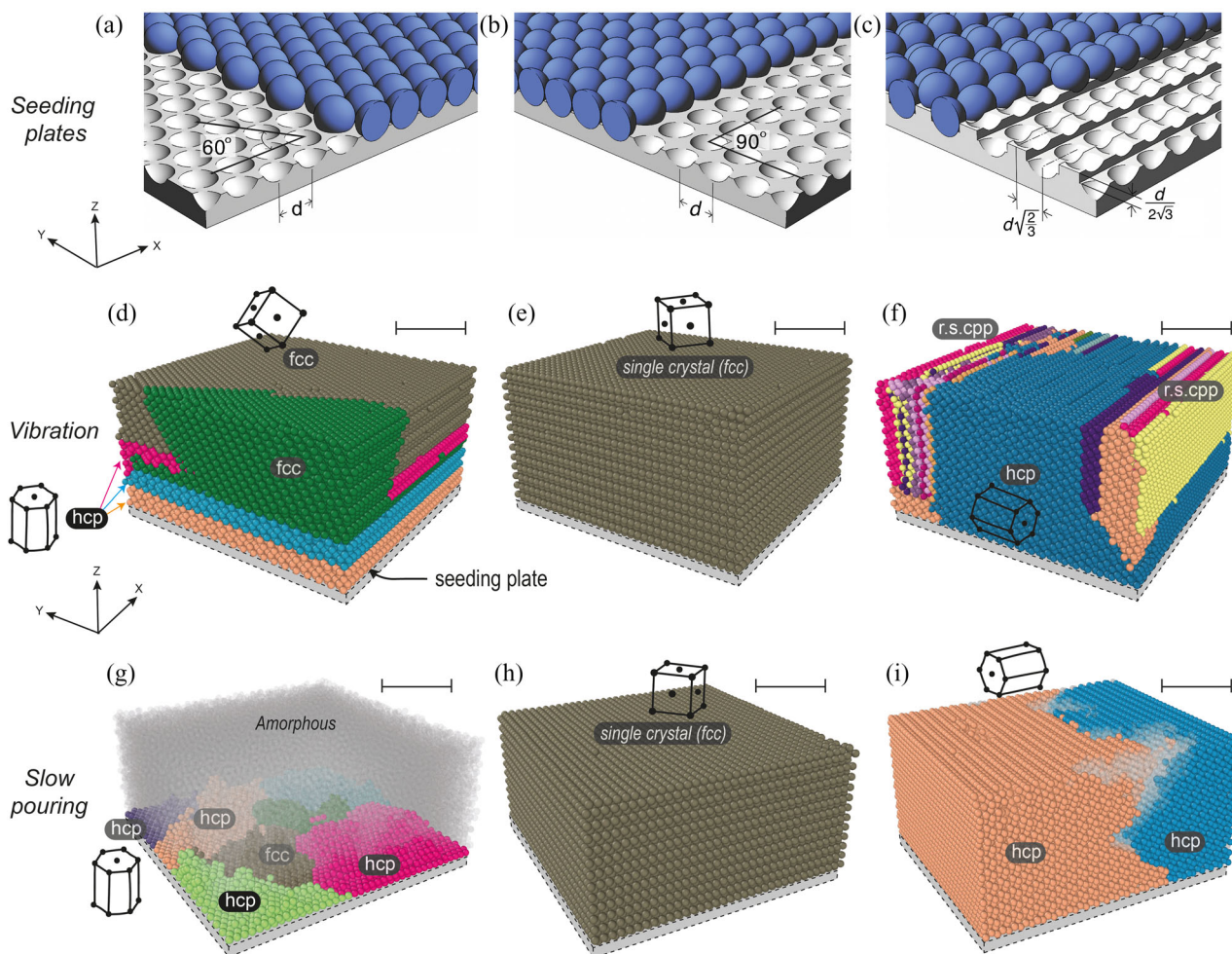


FIGURE 7 Three-dimensional sketches to show the seeding layers. The (a) $\{111\}$ close-packed seeding plane, (b) $\{100\}$ fcc seeding plane, and (c) the $\{10\bar{1}0\}$ prismatic plane of the hcp crystal forming a seeding plane. In each case, we mark the global (X, Y, Z) co-ordinate system such that vibration is along the X -direction and gravity is along the Z -direction. (d–i) XCT reconstructions of the arrangements of the balls with the (d,g) $\{111\}$ close-packed plane, (e,h) $\{100\}$ fcc plane, and (f,i) $\{10\bar{1}0\}$ prismatic plane of the hcp crystal serving as seeding layers. The fcc and hcp unit cells are sketched-in to show the crystal orientations with r.s.c.p.p. denoting randomly stacked close-packed planes. (d–f) show the XCT visualized steady-state arrangements induced by vibration with $f = 20$ Hz and $a = 2$ mm, while (g–i) are the equivalent arrangements resulting from slow pouring using the setup in Figure 1d (no vibration). The XCT images of the balls have been colored to better illustrate the grain structure. Scale bar 25 mm

Improving crystallization via seeding layers

Starting from an amorphous arrangement, the development of vibration-induced crystallinity is most efficient for $f > f_{\text{crit}}$. Under these circumstances, crystallinity grows from the base of the box induced by first the development of a close-packed layer at the base; recall Section “Growth of the crystal structure”. This is consistent with a large body of data on seeding of atomic crystals.³⁸ However, the role of seeding remains unclear in assemblies of hard spheres, where gravity plays a critical role.

We consider three different seeding arrangements motivated by planes through the fcc and hcp crystal structures. In defining the seeding planes, we draw a plane through a set of crystallographic points (the centers of the balls in this case) and the seeding plane is then defined by all the balls that the plane intersects. We choose three seeding planes:

- (i) The close-packed $\{111\}$ plane[†] (Figure 7a), which we have seen tends to develop (with defects) on the base of box in the absence of seeding. The $\langle 110 \rangle$ direction was aligned with the X -direction along which the box was vibrated.
- (ii) The $\{100\}$ plane in the fcc crystal (Figure 7b) with the $\langle 010 \rangle$ direction aligned with the X -direction along which the box was vibrated.
- (iii) The prismatic $\{10\bar{1}0\}$ plane in the hcp crystal (Figure 7c) with the $\langle 11\bar{2}0 \rangle$ slip direction aligned with the X -direction along which the box was vibrated. Unlike the previous two cases, balls on this seeding plane are at two Z -levels as seen in Figure 7c.

[†] Close-packed planes are present in both the fcc and hcp crystals and here we have used the fcc crystal to denote this plane.

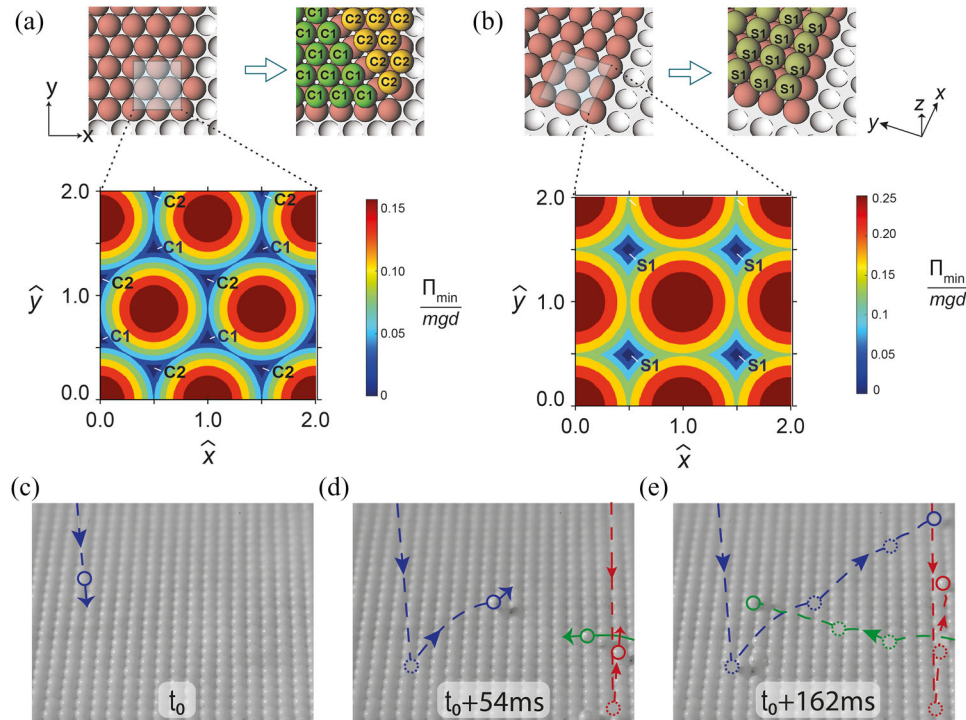


FIGURE 8 Contours of the normalized gravitational potential energy $\bar{\Pi}_{\min}$ in the $X - Y$ plane using normalized co-ordinates $\hat{x} \equiv x/d$ and $\hat{y} \equiv y/d$ for the (a) {111} close-packed plane and (b) {100} fcc plane serving as the seeding layers. The insets show the arrangements of the seeding layer and the subsequent layers. In (a), the two families C_1 and C_2 of stable equilibrium sites are marked. (c–e) Sequence of high-speed photographs showing balls dropped on the {100} fcc plane exploring available equilibrium sites. The time stamps show the timescale of the photographs with the time $t = t_0$ in the first image (c). In the images, we mark a few balls as they explore the available sites. Balls at the current time are shown using a solid circle, while balls at previous times when they touch the surface layer are shown using a dashed circle to give a sense of the history of the motion of the balls

While the motivation for the close-packed plane is that it seems to be naturally induced (Figure 5d), the other two choices are driven by our desire to preferentially induce fcc and hcp crystals, respectively, with gravity providing the required directional bias. The box with the seeding base layer was subjected to vibration at $f = 20$ Hz and amplitude $a = 2$ mm for $N = 3000$ cycles by when a steady-state arrangement forms.

We include the XCT reconstructions of the steady-state arrangements of the balls for the three seeding arrangements in Figures 7d–f. In all cases, we only show a central portion of packings with approximately 10 layers removed from the four sides and five layers from the top of the box to eliminate edge effects. The coloring of the balls denotes the different grains with the grain structures. First, consider the {111} close-packed seeding arrangement (Figure 7d). The arrangement is qualitatively like that in the absence of seeding (Figure 4a) with a mixture of fcc and hcp grains and the grains all oriented with the close-packed planes lying in the $X - Y$ plane of the box. The packing dramatically changes when the {100} plane is used as the seeding layer (Figure 7e). We now obtain an fcc single crystal oriented with the {100} plane in the $X - Y$ plane of the box and no defects present other than a few vacancies; see XCT slices in Figure S4a,c. When the $\{10\bar{1}0\}$ plane of the hcp crystal is used as the seeding layer, we obtain only hcp grains (Figure 7f). However, now in addition to vacancy defects, we also have randomly stacked close-packed planes (r.s. cpp) in the $X - Z$ plane of the

box (Figure 7f). These close-packed planes have slipped by about half a ball diameter with respect to each other, thereby, preventing the development of an hcp single crystal. The immediate question that arises is: what constitutes a good seeding in the context of a dry granular assembly of hard spheres and why the {100} plane results in a pure fcc single crystal?

Gravitational potential energy is the only energy present in the static granular assembly comprising hard spheres. We thus anticipate that the gravitational potential energy landscape plays a crucial role in the arrangements that the balls assume. First, consider the {111} close-packed seeding arrangement in the $X - Y$ plane (Figure 8a). Given this seeding layer, what positions will balls poured on this layer assume, that is, what is the next layer of balls that will form? To understand this, recall that the potential energy of a hard sphere (ball) placed on this seeding layer is $\Pi \equiv mgh$, where h is the height of the centre of the spherical ball measured with respect to an arbitrary datum. This potential energy is a function of the position (x, y) of the ball center in the $X - Y$ plane. We define $\Pi_{\min}(x, y) = mgh_{\min}$, where h_{\min} is the minimum value of h at the given position (x, y) (when the ball is in contact with the balls in the layer below). We include contours of $\bar{\Pi}_{\min} \equiv \Pi_{\min}/(mgd)$ in Figure 8a using normalized co-ordinates $\hat{x} \equiv x/d$ and $\hat{y} \equiv y/d$ (the datum for h is defined such that the minimum value $\bar{\Pi}_{\min}$ over all (x, y) is zero). The balls are in stable equilibrium at locations of minimum $\bar{\Pi}_{\min}$ in the $X - Y$ plane. Two families of stable equilibrium sites are observed

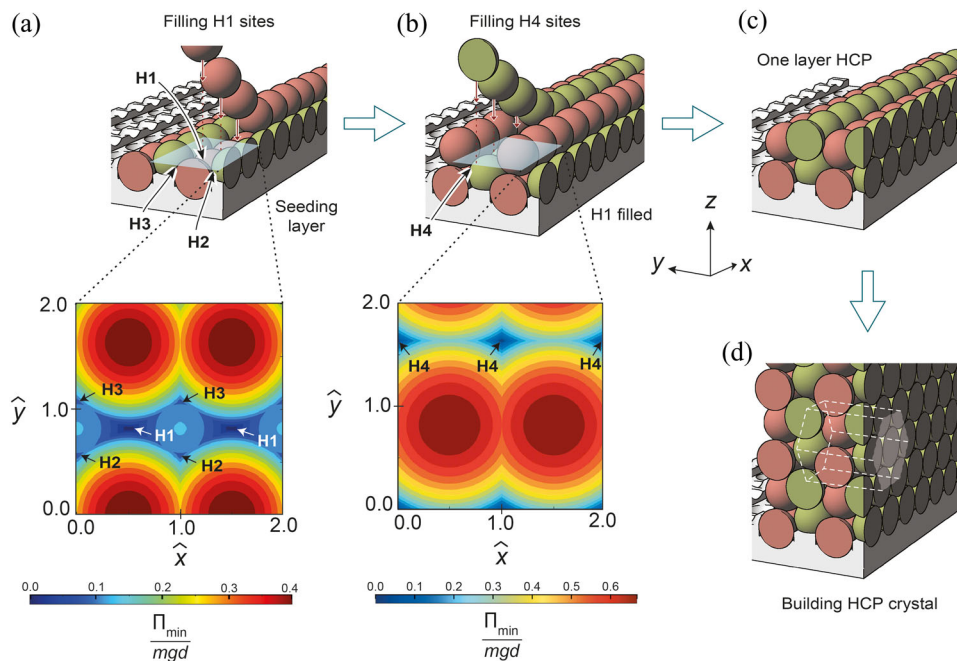


FIGURE 9 (a) Contours of the normalized gravitational potential energy $\bar{\Pi}_{\min}$ for the $\{10\bar{1}0\}$ prismatic plane of the hcp crystal serving as the seeding layer. The three families of stable equilibrium sites H_1 , H_2 , and H_3 are marked. The inset shows the arrangement resulting by filling the global minimum energy sites H_1 on the seeding layer. (b) The modified energy landscape after filling all the H_1 sites on the seeding layer. A single family of stable equilibrium sites H_4 is present in this modified energy landscape. (c) Resulting arrangement of the balls after filling the H_1 and H_4 sites. (d) The continued building of the hcp crystal with the orientation of the hcp unit cell indicated by dashed lines

and labeled C_1 and C_2 in Figure 8a. Both these sites have $\bar{\Pi}_{\min} = 0$ but adjacent C_1 and C_2 sites cannot be occupied simultaneously as they are separated by a distance less than d . Thus, the layer on top of the seeding layer can be formed by either occupying C_1 or C_2 sites creating a new close-packed layer, and the procedure repeats to build a crystal. Since there is no energetic preference for occupancy of either of the two families of sites, the formation of a C_1 or C_2 next layer is random. Consequently, there is an equal likelihood of obtaining either an ABAB arrangement (hcp crystal) or an ABCABC arrangement (fcc crystal) as seen in the observations. Moreover, even within a layer, we can have different regions, where C_1 and C_2 are occupied and separated by a defect boundary as shown in the inset of Figure 8a: this will be further discussed in Section “Crystallization without vibration” in the context of crystallization without vibration. Next, consider the $\{100\}$ seeding layer. The corresponding contours of $\bar{\Pi}_{\min}$ are included in Figure 8b and now clearly, there is only one family of stable equilibrium sites for the balls. Filling all these sites results in an arrangement identical to the seeding layer and the process repeats to build an fcc crystal rotated with respect to that in Figure 8a. This uniqueness of stable equilibrium sites results in the formation of the fcc single crystal seen in Figure 7e.

Finally, consider the $\{10\bar{1}0\}$ seeding layer. The fact that not all balls are at the same z -level makes this more complex to understand. Contours of $\bar{\Pi}_{\min}$ for balls deposited on the seeding layer are included in Figure 9a (the arrangement of the balls on seeding layer is shown in the inset). The energy landscape of this is complex with three families of stable equilibrium sites available labeled H_1 , H_2 , and H_3 in Figure 9a such that adjacent sites from different families cannot be simultane-

ously occupied. The H_1 sites have the minimum energy, and filling all the H_1 sites first will create the new arrangement seen in Figure 9a. This new layer, unlike in the previous two cases, is not identical to the initial seeding layer, and thus, further filling is governed by a new energy landscape. This new energy landscape is shown in Figure 9b with h again defined with respect to a datum such that the minimum value of $\bar{\Pi}_{\min}(x, y) = 0$ on this new plane. This new energy landscape has a single family of stable equilibrium sites (labeled H_4) and filling those sites recreates the initial seeding layer (Figure 9c), and the process of crystal growth then progresses in this two-step manner to generate a perfect hcp crystal (Figure 9d). However, as was clear from Figure 9a, the process of filling the available sites on the initial seeding layer is nonunique: filling of either all the H_2 or H_3 sites (which are stable equilibrium sites but at a higher energy level compared to the H_1 sites) will also result in the growth of an hcp crystal but one that is slipped along the vertical close-packed plane with respect to the hcp crystal below the seeding plane. It is this nonuniqueness of the available equilibrium sites on prismatic seeding plane that results in the growth of a structure dominated by the hcp crystal but with some randomly stacked close-packed planes (Figure 7f).

We hypothesize that gravity-biased growth of a single crystal requires two conditions to be met: (1) the energy landscape of the seeding plane needs to have a single family of stable equilibrium sites and (2) all balls on the seeding plane must be at the same z -level so that the seeding plane is recreated by filling these equilibrium sites and the process can then repeat itself. While such a plane exists for the fcc crystal (the $\{100\}$ plane), no such plane exists for the hcp crystal: the lower

degree of symmetry in the hcp crystal means that only the close-packed seeding plane has all balls at the same z -level, and this seeding plane does not have a unique family of equilibrium sites (Figure 8a).

Crystallization without vibration

While the development of an fcc crystal from the $\{100\}$ seeding plane occurs due to the uniqueness of the equilibrium site, vacancies are still observed in the fcc single crystal (Figure S4a,c). These vacancies are energetically unfavorable, so we surmise that they exist because they have been trapped during the formation of the crystal from the initial random arrangement with the imposed vibrations insufficient to “anneal” the vacancies out. Similarly, from a purely energetic perspective, slip defects should also not be present when an hcp crystal is seeded from the prismatic plane as these defects require balls to occupy the higher H_2 or H_3 potential energy sites. Given this, it was natural to ask whether slow growth of the crystals from the $\{100\}$ and $\{10\bar{1}0\}$ seeding layers can reduce/eliminate such defects.

To investigate this, we designed a system whereby we uniformly and slowly poured balls onto a seeding plane that formed the bottom of the box. The box was not vibrated. To ensure spatially uniform spreading of the balls, two layers of a square mesh were placed at the top of the box (Figure 1d). The two meshes in the $X - Y$ plane were placed 15 mm apart in the Z -direction and maximally misaligned (Figure 1c). Balls were poured into the box at a rate of $\approx 50,000$ balls/min so that all the 100k balls were poured in ≈ 2 min. Collisions of the balls with the misaligned mesh result in the balls spreading uniformly over the cross-section of the box. The arrangements of the balls were visualized via X-ray tomography after the pouring was completed. The 3D reconstructed arrangements of the balls are included in Figures 7g–i and have layers from the side and the top removed like the images in Figures 7d–f.

Slow pouring of the balls on the $\{111\}$ close-packed seeding plane resulted in an amorphous arrangement of the balls above a few layers from the base seeding plane (Figure 7g). This is understood as follows. Two energetically equally favorable families of sites, C_1 and C_2 , exist on the $\{111\}$ close-packed plane (Figure 8a). Thus, we would expect slow pouring to result in similar occurrence of C_1 and C_2 regions. Wherever they meet, an incoherent boundary will exist between them (Figure 8a). This is precisely what is observed (see XCT reconstruction in Figure S5 of the layer immediately above the seeding layer). This process repeats itself in the next layer with further defects so that very soon correlation with the original seeding layer is completely lost and an amorphous arrangement ensues (see XCT reconstruction in Figure S5 of the fourth layer above the seeding layer). Next, consider slow pouring on the $\{100\}$ seeding layer. Not only is a pure fcc single crystal observed to develop (Figure 7h), but this crystal has a vacancy fraction $\approx 0.02\%$ compared to the vacancy fraction of $\approx 0.08\%$ that develops in the vibration-induced assembly; compare the XCT slices through the crystals in Figure S4. This is because slow pouring allows the attainment of nearly the lowest energy structure to develop with minimal trapping of vacancies compared to the situation in the vibration-induced assembly of an initially

amorphous structure. The role of the kinetic energy of the falling balls in helping the balls sample sites to find an equilibrium position in helping the process of epitaxial growth has been recognized: high-speed photographs (taken using an interframe time of 2 ms) of balls dropping on the $\{100\}$ seeding layer shown in Figures 8c–e clarify this process showing the mechanism by which balls explore available equilibrium sites.

Similarly, slow pouring over the $\{10\bar{1}0\}$ seeding layer also significantly reduces the number of randomly stacked close-packed planes that form, with the image in Figure 7i showing a structure with only two hcp grains separated by an amorphous region. Thus, while we do not obtain a single crystal in this case, the defects are reduced compared to when an amorphous assembly is crystallized via vibration (Figure 7f). We rationalize this by noting that while the seeding layer does not have a unique family of equilibrium sites, the H_1 family is energetically favorable – slow pouring allows these minimum energy sites to be preferentially occupied, while vibration-induced crystallization of an initially amorphous assembly results in ball trapping in the stable, but higher energy H_2 and H_3 sites, resulting in the defects seen in Figure 7f. It should be noted that of the three seeding templates that were studied, only $\{100\}$ seeding layer consistently produces defect-free single crystals due to the uniqueness of equilibrium sites. Since the potential energy landscape of successive layers is identical, there is no inherent limit to the size of the crystal that can be grown by this process, as long as the lateral dimensions are large enough to prevent wall effects.

Epitaxial growth of a metastable crystal

Close-packed arrangements, such as the fcc and hcp crystals, form under the influence of gravity as the mono-size hard spheres pack to the theoretical maximum volume fraction of 74% and, therefore, minimize the gravitational potential energy of the entire assembly. However, the energy landscape in Figure 8b suggests a route to the assembly of a cubic but nonclose-packed body centered cubic (bcc) arrangement. We now consider a $\{100\}$ plane with crystallographic points (i.e., centers of balls) spaced a distance s apart along both the X and Y -directions as shown in the inset of Figure 10a. When $s = d$, we reduce to the fcc $\{100\}$ plane but an energy landscape with a unique family of stable equilibrium sites exists for spacings in the range $d \leq s \leq \sqrt{3/2}d$. The volume fraction $\bar{\rho}$ occupied by the spheres for arrangements constructed by filling the unique equilibrium sites on the seeding and the subsequent planes is plotted in Figure 10a as a function of s . The spacing $s = 2/\sqrt{3}d$ is a special case as the packing density of the spheres is minimized for this choice of s with the spheres packing to a volume fraction $\bar{\rho} = 0.68$. In fact, for this choice of spacing, the seeding plane is the $\{100\}$ plane of the bcc crystal structure. The XCT visualization of the assembly generated by slow pouring of balls (following the protocol of Section “Crystallization without vibration”) with the $\{100\}$ bcc seeding layer is shown in Figure 10b. Clearly, a bcc single crystal structure is generated with only a few vacancy defects. We emphasize that this bcc arrangement is metastable, that is, it is not the lowest energy structure as it is not closed-packed. Thus, this structure has been

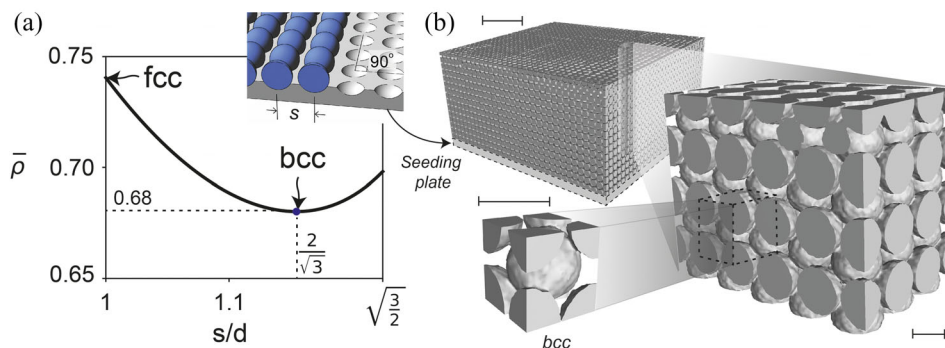


FIGURE 10 (a) Volume fraction $\bar{\rho}$ occupied by spheres as a function of the spacing s on the $\{100\}$ seeding plane for assemblies constructed by occupying the unique equilibrium sites on the seeding plane and subsequent layers. The fcc and bcc arrangements are obtained for specific values of s as indicated. The inset shows the seeding plane and the definition of s . (b) XCT reconstruction of the bcc packing arrangement resulting from slow pouring onto the $\{100\}$ seeding plane with an interball spacing $s = 2/\sqrt{3}d$. The zoom-in insets clearly show the bcc structure of the packing. Scale bar is 20 mm for the full arrangements with 2 mm scale bars for the insets

generated because slow pouring traps the balls in the equilibrium positions on the seeding and subsequent layers. Therefore, such an arrangement even with the correct seeding layer cannot be vibration induced as vibrations will tend to try and assemble the balls into a close-packed arrangement to minimize the overall energy of the entire assembly. In fact, vibration of the assembly with the bcc seeding layer was found to result in a highly defective structure as the assembly has a bcc arrangement near the seeding layer but then transition into an fcc/hcp structure away from the seeding layer with this transition increasing the overall fraction of defects.

CONCLUDING REMARKS

We have investigated the crystallization of a dry assembly of mono-size hard spheres by a combination of experiments, which include visualization via XCT, and discrete element simulations. We demonstrate that the gravitational potential energy of the spheres dictates their assembly. Crystallization under imposed vibration but with no seeding is governed by the ratio of the imposed acceleration to the acceleration due to gravity. However, single crystals cannot form under these circumstances as the gravitational potential energy of the fcc and hcp arrangements makes them equally likely, and this results in an arrangement with defects separating the fcc and hcp grains.

The critical role of gravity in the crystallization process was exploited to epitaxially grow crystals from a horizontal seed layer. We demonstrate that a single crystal with only limited vacancy defects can be self-assembled from a seed layer mimicking the $\{100\}$ fcc plane. In fact, this self-assembly can be purely gravity driven and does not require imposed vibration. Modifying the $\{100\}$ fcc seeding plane to that of the bcc crystal permits the assembly of a bcc single crystal. However, the bcc crystal is nonclose-packed and, therefore, is metastable and can only be gravity assembled in the absence of vibration. Using the gravitational energy landscape of the seeding layers, we argue that an energy landscape with a unique family of equilibrium sites is needed to ensure the formation of a single crystal. Our results provide mechanistic insights into the dry self-assembly of mono-size spheres that can

serve as templates for the manufacture of architected materials, such as inverse opals.

MATERIALS AND METHODS

Materials and apparatus

Spherical cellulose acetate balls[‡] with a nominal diameter $d = 2$ mm were used in all the experiments. These high precision balls had a Gaussian distribution of diameters (as measured over a sample of 100k balls) with a mean diameter 2.01 mm and standard deviation 0.020 mm (Figure S1). The vibration setup (Figure 1c) comprises a Perspex box, an electromagnetic shaker (LDS model V406), a power amplifier, and a signal generator, which determines the output waveform of the oscillatory motion from the shaker. The Perspex box with the balls was supported on pin rollers and coupled to the shaker via a rigid joint (Figure 1c) that permitted only one-dimensional motion of the box. The voltage of the amplifier and output of the signal generator together control the oscillations of the box. We performed a series of calibration experiments to calibrate the settings of amplifier and signal generator to achieve the required waveform. Oscillations of the box were observed via high-speed photography using a Phantom v1610 digital camera[§] capturing images at a frame rate 20 times higher than the vibration frequency (and an exposure time of 20 μ s). The power amplifier voltage was then adjusted to achieve the required vibration amplitude of the box. This procedure was repeated for the full range of frequencies ($8 \text{ Hz} \leq f \leq 25 \text{ Hz}$) and amplitudes ($1.5 \text{ mm} \leq a \leq 4 \text{ mm}$) investigated here.

Vibration protocol

The inside of the Perspex box was coated with a conducting spray (Licron Crystal ESD safe coating by Techspray) and then grounded via a copper wire to reduce electrostatic attraction between the balls and

[‡] Precision Plastic Ball Co Ltd, U.K.

[§] Vision Research, Priory Business Park, Stannard Way, Bedford, MK44 3RZ, UK.

the sides of the box. We also coated all the balls with antistatic spray (Ambersil) to reduce electrostatic attraction between the balls. Both the conducting and antistatic coatings eroded over time, and hence, these coatings were reapplied after approximately every 50,000 cycles. The 100k balls were first poured into the box and the arrangement of balls randomized by first putting a lid on the box and then turning it topsy-turvy a few times. This resulted in a dense random packing of the balls inside the Perspex box with approximately a 60% by volume packing of the balls. The box was then attached to the shaker setup (Figure 1c) with the frequency of the signal generator and the voltage of the amplifier set to the values calibrated to give the desired oscillatory output. The power amplifier was then switched on and this initiated the horizontal oscillations of the box without an initial jerk. Vibration amplitude and frequency were periodically monitored using the high-speed camera and an oscilloscope, respectively. A stopwatch was used to monitor time and the power amplifier was switched-off after the desired number of cycles were attained. The capacitive decay of the output power from the amplifier then brought the box to rest without a jerk. The box was then carefully transferred for visualization via XCT: an example of XCT image of the box with the 100k balls prior to vibration is included in Figure 1e.

Visualization via XCT and image analysis

The vibration experiments were periodically interrupted to visualize the development of the crystalline structure of the assembly. The X-ray scans were acquired using the Nikon XTH 225 ST CT system with X-rays generated from a Tungsten filament at ~ 185 kV–90 μ A projected onto a 2000 pixel \times 2000 pixel detector. A resolution of 200 μ m was achieved using geometric magnification and the acquired XCT dataset post-processed in the commercial software VGStudioMax 3.5. Each ball in the granular assembly was segmented from the surrounding air using a surface determination approach with a merger tolerance of 1%. A general FP analysis was then performed on the balls to find their centers and diameters. The FP analysis was also used to analyze the voids between the balls using an algorithm that successively fits spheres into the void volume until spheres of diameters approaching the XCT resolution (i.e., ~ 200 μ m) almost fill the void space. This allows us to extract the distribution of void volumes and correlate these volumes to the known volumes of tetrahedral and octahedral voids that are present in crystalline assemblies of mono-size spheres. To determine the crystal arrangements and crystallinity fractions, ball positions and diameters were exported from the XCT dataset to the open-source software LAMMPS and the polyhedral template matching (PTM)⁴⁰ algorithm used to infer the local crystal structures. The open-source software Ovito was used to visualize the granular assembly.

The discrete element model

Three-dimensional simulations are performed using mono-size spherical balls of diameter d and mass m_p . Here, for consistency with the

DEM literature, we shall refer to the balls as particles. The soft-particle contact model (Figure S6a), introduced by Cundall and Strack,³⁶ and extended to large-scale simulations by Campbell and Brennen⁴¹ and by Campbell,⁴² accounted for both interball interactions and the interactions of the balls with the sides of the box. The interparticle contact law comprises:

- (i) A linear spring with spring constant K_n and a linear dashpot with damping constant γ_n connected in parallel, governing the contact force–displacement relation in the direction connecting the ball centers.
- (ii) A linear spring of constant K_s and Coulomb friction coefficient μ connected in series, governing the tangential contact relationship.

Let r denote the distance of separation of the ball centers or the distance between the ball center and the contact point on the sides of the box. Then, the particle interpenetration for particle–particle and particle–box contact is given by $\delta_n = r - d$ and $\delta_n = r - d/2$, respectively, so that the normal force during active contact ($\delta_n < 0$) is

$$F_n = K_n \delta_n + m_{\text{eff}} \gamma_n \dot{\delta}_n. \quad (1)$$

Here, m_{eff} is the reduced mass of the two contacting bodies. For impacts between a pair of balls, $m_{\text{eff}} = m_p/2$, while for impacts between a ball and the sides of the rigid box, $m_{\text{eff}} = m_p$. The tangential force F_s only exists during an active contact and opposes sliding. It is limited in magnitude to $|F_s| < \mu |F_n|$, where μ is the friction coefficient defined as follows. Denoting the tangential displacement rate between the contacting particles by $\dot{\delta}_s$, the rate of change of the tangential force \dot{F}_s is then given by an elastic–plastic Coulomb type relation with stiffness K_s such that

$$\dot{F}_s = \begin{cases} K_s \dot{\delta}_s & \text{if } |F_s| < \mu |F_n| \text{ or } F_s \dot{\delta}_s < 0 \\ 0 & \text{otherwise} \end{cases} \quad (2)$$

with the initial condition that $F_s = 0$ when contact is first made. The friction coefficient between balls and between the balls and the sides of the box is assumed to be the same. The value of damping constant γ_n dictates the loss of particle kinetic energy during normal collision and is directly related to the coefficient of restitution e according to

$$e = \exp \left[-\pi \left(\frac{8 K_n}{\gamma_n^2 m_p} - 1 \right)^{-1/2} \right]. \quad (3)$$

The collision time t_e for individual binary collisions then follows from (1) as:

$$t_e = -2 \frac{\ln(e)}{\gamma_n}, \quad (4)$$

and thus, in the limit of plastic collisions with $e \rightarrow 0$, the contact time $t_e \rightarrow \infty$. Newton's equations for both the translational and rotational motions of the particles were integrated using a Verlet time-integration scheme (Newark–Beta with $\beta = 0.5$). The time-step for

integration was taken to be less than $t_e/15$ to ensure accurate integration of the equation of motions. We emphasize that acceleration $g \equiv \alpha g$ due to gravity is included in the calculations so that a translational acceleration $-\alpha g$ is added in the Z -direction. Here, $g \approx 10 \text{ ms}^{-2}$ is the acceleration due to gravity and α is a dimensionless parameter that specifies the gravitational strength and used as a parameter to numerically understand the role of gravity.

Simulation procedure

The first step of the simulations was generation of the initial amorphous assembly of M balls in the box. This was carried out as follows. A slab of thickness $h = 15d$ was positioned at a height $80d$ above the base of the box as shown in Figure S6b. Balls were randomly positioned inside this slab so that a volume fraction $\bar{\rho}_{\text{fill}} = 0.1$ of balls was maintained in the slab and the balls permitted to fall into the box under the influence of gravity. Thus, as balls leave the slab, new initially stationary balls were introduced at random locations within the slab until a total of M balls were in the system. The interactions between the balls and the sides of the box during the step were modeled as described above. Collisions between the balls and the balls and the sides of the box resulted in the balls rearranging and coming to rest due to the dissipative nature of the interactions (1) and (2). This stationary assembly was almost amorphous in line with the initial assembly in the experiments. In the second step, the box was subjected to shaking by imposing a displacement $u = a(1 - \cos(\omega t))$ to the rigid box in the X -direction with displacements of the box in the Y and Z -directions set to zero. Here, time $t = 0$ corresponds to the instant the shaking commenced. This protocol adequately captures the experimental shaking protocol. The imposed shaking was periodically stopped, and the balls allowed to settle until they came to rest. The arrangement of the balls was then analyzed using a protocol identical to that used to analyze the XCT images with PTM used to analyze the crystal structure given the centers and radii of all the spherical balls in the box. The analysis of the void volumes from the simulations required us to first generate 2D slices of the ball arrangements predicted by the simulations as DICOM images. To improve the deficiencies in interpolation between slices, three sets of slices were generated for every dataset (perpendicular to the X , Y , and Z directions, respectively) with lateral resolution $\sim 100 \mu\text{m}$ and with the spacing of slices $\sim 150 \mu\text{m}$. The DICOM datasets were imported into VGStudioMax 3.5 and combined into a single 3D volumetric data file. Subsequently, the FP analysis was used to extract the void volumes in a manner identical to that used for the XCT dataset.

Model parameters

All calculations presented here used the following reference properties for the $M = 10^5$ spherical balls of diameter $d = 2 \text{ mm}$. The density of the material of the balls was measured to be $\rho_s = 1270 \text{ kgm}^{-3}$, and thus, all balls in the simulations were assumed to be made from a

solid of density ρ_s . The ball-ball and ball-box contact model is specified by four parameters K_n , e , $K_s = (2/7)K_n$, and μ . Over a wide range of realistic parameters, K_n and e do not affect the predictions; see Figure S3a, where we show the effect of K_n , e , d as well as ρ_s on level of crystallinity developed at steady state. All results presented in the main text used $K_n = 10 \text{ N cm}^{-1}$ and $e = 0.6$. However, our computational results (Figure S3b) show that the friction coefficient does have a large influence on the vibrational frequency required to induce crystallization. We thus conducted detailed measurements of μ (Figures S7 and S8) and all calculations in the main text used the measured value of the static friction coefficient $\mu = 0.2$. In all cases, we set $g = 10 \text{ ms}^{-2}$ but vary the gravitational strength via α , where $\alpha = 1$ corresponds to standard gravitational conditions.

ACKNOWLEDGMENTS

The authors are grateful to Army Research Office (ARO) for their financial support through grant number W911NF-19-1-0075 on scalable growth of crystalline materials and their inverses (program managers Dr Mike Bakas and Dr Jim Harvey). A.J.D.S. was supported by Cambridge-India Ramanujan scholarship from the Cambridge Trust and the Science and Engineering Research Board, Govt. of India. I.G. is supported by the Ashby PhD Scholarship by the Department of Engineering, University of Cambridge.

CONFLICT OF INTEREST

The authors declare no conflict of interest.

ETHICS STATEMENT

No animals were involved in the research.

AUTHOR CONTRIBUTIONS

Ivan Grega: Data curation; formal analysis; investigation; methodology; validation; visualization; writing—original draft; writing—review and editing. Angkur Shaikeea: Data curation; formal analysis; investigation; methodology; validation; visualization; writing—original draft; writing—review and editing. Haydn Wadley: Conceptualization; funding acquisition; methodology; writing—review and editing; Vikram Deshpande: Conceptualization; funding acquisition; methodology; project administration; supervision; writing—original draft; writing—review and editing.

DATA AVAILABILITY STATEMENT

The data that support the findings of this study are available from the corresponding author upon reasonable request.

PEER REVIEW

The peer review history for this article is available at <https://publons.com/publon/10.1002/ntls.20220007>

ORCID

Ivan Grega  <https://orcid.org/0000-0002-0163-7009>

Vikram S. Deshpande  <https://orcid.org/0000-0003-3899-3573>

REFERENCES

1. Fleck NA, Deshpande VS, Ashby MF. Micro-architected materials: past, present and future. *Proc R Soc A*. 2010;466:2495-2516.
2. Spadaccini C. Additive manufacturing and processing of architected materials. *MRS Bull.* 2019;44:782-788.
3. Wadley HNG, Fleck NA, Evans AG. Fabrication and structural performance of periodic cellular metal sandwich structures. *Comp Sci Tech.* 2003;63:2331-2343.
4. Velev OD, Jede TA, Lobo RF, Lenhoff AM. Porous silica via colloidal crystallization. *Nature.* 1997;389:447-448.
5. Wijnhoven JEGJ, Vos WL. Preparation of photonic crystals made of air spheres in titania. *Science.* 1998;281:802-804.
6. Vlasov YA, Bo XZ, Sturm JC, Norris DJ. On-chip natural assembly of silicon photonic bandgap crystals. *Nature.* 2001;414:289-293.
7. Bartlett PN, Baumberg JJ, Coyle S, Abdelsalam ME. Optical properties of nanostructured metal films. *Faraday Discuss.* 2004;125:117-132.
8. Dolan JA, Wilts BD, Vignolini S, Baumberg JJ, Steiner U, Wilkinson TD. Optical properties of gyroid structured materials: from photonic crystals to metamaterials. *Adv Opt Mater.* 2015;3:12-32.
9. Pikul JH, Long JW. Architected materials for advanced electrochemical systems. *MRS Bull.* 2019;44:789-795.
10. Pikul JH, Zhang HG, Cho J, Brown PV, King WP. High-power lithium ion microbatteries from interdigitated three-dimensional bicontinuous nanoporous electrodes. *Nat Commun.* 2013;4:1732.
11. Pikul JH, Özerinç S, Liu B, et al. High strength metallic wood from nanostructured nickel inverse opal materials. *Sci Rep.* 2019;9:719.
12. van Blaaderen A, Ruel R, Wiltzius P. Template-directed colloidal crystallization. *Nature.* 1997;385:321-324.
13. Pusey PN, van Megen W. Phase behaviour of concentrated suspensions of nearly hard colloidal spheres. *Nature.* 1986;320:340-342.
14. Harland JL, Henderson SI, Underwood SM, van Wegen W. Observation of accelerated nucleation in dense colloidal fluids of hard sphere particles. *Phys Rev Lett.* 1995;75:3572.
15. Davis KE, Russel WB, Glantschnig WJ. Disorder-to-order transition in settling suspensions of colloidal silica: X-ray measurements. *Sci Rep.* 1989;245:507-510.
16. Ackerson BJ. Shear induced order and shear processing of model hard sphere suspensions. *J Rheol.* 1990;34:553-590.
17. Scott GD. Packing of equal spheres. *Nature.* 1960;188:908-909.
18. Scott GD, Kilgour DM. The density of random close packing of spheres. *J Phys D, Appl Phys.* 1969;2:863-866.
19. German RM. *Particle packing characteristics*. Metal Powder Industries Federation; 1989.
20. Owe Berg TG, McDonald RL. The packing of spheres. *Powder Technol.* 1969;3:183-188.
21. Li CX, An XZ, Yang RY, Zou RP, Yu AB. Experimental study on the packing of uniform spheres under three-dimensional vibration. *Powder Technol.* 2011;208:617-622.
22. Knight JB, Fandrich CG, Lau CN, Jaeger HM, Nagel SR. Density relaxation in a vibrated granular material. *Phys Rev E.* 1995;51:3957-3963.
23. An XZ, Li CX, Yang RY, Zou RP, Yu AB. Experimental study of the packing of mono-sized spheres subjected to one-dimensional vibration. *Powder Technol.* 2009;196:50-55.
24. An X, Li C. Experiments on densifying packing of equal spheres by two-dimensional vibration. *Particuology.* 2013;11:689-694.
25. An X, Yang R, Dong K, Yu A. DEM study of crystallization of monosized spheres under mechanical vibrations. *Comp Phys Comm.* 2011;182:1989-1994.
26. Yu AB, An XZ, Zhou RP, Yang RY, Kendall K. Self-assembly of particles for densest packing by mechanical vibration. *Phys Rev Lett.* 2006;97:265501.
27. Wang D, An X, Gou D, Zhao H, Wang L, Huang F. DEM construction of binary hard sphere crystals and radical tessellation. *AIP Adv.* 2018;8:105203.
28. An XZ, Yang RY, Zou RP, Yu AB. Effect of vibration condition and inter-particle frictions on the packing of uniform spheres. *Powder Technol.* 2008;188:102-109.
29. Nowak ER, Knight JB, Povinelli ML, Jaeger HM, Nagel SR. Reversibility and irreversibility in the packing of vibrated granular material. *Powder Technol.* 1997;94:79-83.
30. Carvente O, Ruiz-Suárez JC. Crystallization of confined non-Brownian spheres by vibrational annealing. *Phys Rev Lett.* 2005;95:018001.
31. Amirifar R, Dong K, Zeng Q, An X. Bimodal self-assembly of granular spheres under vertical vibration. *Soft Matter.* 2019;15:5933-5944.
32. Nahmad-Molinari Y, Ruiz-Suárez JC. Epitaxial growth of granular single crystals. *Phys Rev Lett.* 2002;89:264302.
33. Pouliquen O, Nicolas M, Weidman PD. Crystallization of non-Brownian spheres under horizontal shaking. *Phys Rev Lett.* 1997;79:3640.
34. Mullins WW, Sekerka RF. Stability of a planar interface during solidification of a dilute binary alloy. *J Appl Phys.* 1964;35:444-451.
35. Frenkel D. Order through entropy. *Nat Mater.* 2015;14:9-12.
36. Cundall PA, Strack ODL. A discrete numerical model for granular assemblies. *Géotechnique.* 1979;29:47-65.
37. Thompson AP, Aktulga HM, Berger R, et al. LAMMPS — a flexible simulation tool for particle-based materials modeling at the atomic, meso, and continuum scales. *Comp Phys Comm.* 2022;271:10817.
38. Parambil JV, Heng JYY. Seeding in crystallisation. In: Roberts K, Docherty R, Tamura R, eds. *Engineering Crystallography: from Molecule to Crystal to Functional Form*. NATO Science for Peace and Security Series A: Chemistry and Biology. Springer; 2017. p 235-245.
39. Panaitescu A, Kudrolli A. Epitaxial growth of ordered and disordered granular sphere packings. *Phys Rev E.* 2014;90:032203.
40. Larsen PM, Schmidt S, Schiøtz J. Robust structural identification via polyhedral template matching. *Model Simul Mater Sci Eng.* 2016;24:055007.
41. Campbell CS, Brennen CE. Chute flows of granular material: some computer simulations. *J Appl Mech.* 1985;52:172-178.
42. Campbell CS. Granular shear flows at the elastic limit. *J Fluid Mech.* 2002;465:261-291.

SUPPORTING INFORMATION

Additional supporting information can be found online in the Supporting Information section at the end of this article.

How to cite this article: Grega I, Shaikeea AJD, Wadley HNG, Deshpande VS. Gravity enables self-assembly. *Nat Sci.* 2022;e20220007. <https://doi.org/10.1002/ntls.20220007>